AIAA JOURNAL
Vol. 49, No. 1, January 2011

Effect of Mach Number on Flow Past Microramps

S. Lee* and E. Loth†
University of Illinois at Urbana–Champaign, Urbana, Illinois 61801
and
N. J. Georgiadis‡ and J. R. DeBonis‡
NASA John H. Glenn Research Center at Lewis Field, Cleveland, Ohio 44135

DOI: 10.2514/1.J050267

Micro vortex generators have the ability to alter the near-wall structure of compressible turbulent boundary layers to provide increased mixing of high-speed fluid, such that the boundary layer remains healthy even with some disturbance imparted to the flow. Because of their small size, micro vortex generators are embedded in the boundary layer and may provide reduced drag when compared with traditional vortex generators. To examine their potential, a detailed computational study was undertaken of microramps with a height of $h \sim 0.5\delta$ in a supersonic boundary layer at $M = 1.4$, 2.2, and 3.0. The large eddy simulation results indicate that microramps have a greater impact at lower Mach number near the device, but this influence decays faster than at the higher Mach numbers. This may be due to the additional dissipation caused by the primary vortices with smaller effective diameter at the lower Mach number, such that their coherency is easily lost, causing the streamwise vorticity and the turbulent kinetic energy to decay quickly. The normal distance between the vortex core and the wall had similar growth, indicating weak correlation with the Mach number; however, the spanwise distance between the two counter-rotating cores further increases with lower Mach number.

Nomenclature

a	=	speed of sound
$\mathrm{d}t$	=	time increment for integration
$\mathrm{d}t^*$	=	nondimensional $\mathrm{d}t$, same as Courant–Freidrichs–Lewy number
$\mathrm{d}x$	=	spatial increment in streamwise direction
$\mathrm{d}y$	=	spatial increment in normal direction
$\mathrm{d}z$	=	spatial increment in spanwise direction
h	=	microramp height
K	=	spatial average of time-averaged turbulent kinetic energy
L	=	length of the computational domain
M	=	Mach number
r	=	grid-stretching ratio in normal direction
U_{VD}	=	mean velocity in Van Driest coordinate
U_τ	=	frictional velocity
u	=	instantaneous streamwise velocity
W	=	time- and spatially averaged streamwise vorticity
w	=	width of the microramp
x	=	streamwise distance
Y	=	area center for average streamwise vorticity in y
y	=	normal distance relative to solid wall
Z	=	area center for average streamwise vorticity in z
z	=	spanwise distance relative to center of domain
Γ	=	circulation
Δt	=	time step
Δx	=	streamwise length of computational cell of coarse grid
Δy	=	transverse length of computational cell of coarse grid
Δz	=	spanwise length of computational cell of coarse grid
δ_{ref}	=	boundary-layer thickness at the microramp trailing edge
δ^*_{ref}	=	displacement thickness at the device trailing edge
τ	=	time interval for averaging
τ^*	=	convective flow-through time
υ	=	instantaneous transverse velocity
ω	=	instantaneous spanwise velocity
ω_x	=	streamwise vorticity
$\bar{\ }$	=	time-averaged quantity

Subscripts

dom	=	domain
int	=	integration
rec	=	downstream recycling plane
wall	=	measurement at the wall
∞	=	freestream

Superscripts

$+$	=	dimension in wall units
$'$	=	fluctuation component

I. Introduction

FLOW control application for shock/boundary-layer interaction remains an important technology that requires further investigation. A popular flow control method for supersonic inlet applications is to bleed the flow at the shock impingement region to suppress separations, reducing the boundary-layer thickness and increasing the pressure recovery. However, in order to be effective, bleed has the significant cost of removing a portion of the incoming mass flow [1] that could have otherwise been used in the propulsion system flowpath. This requires larger inlets to compensate for the lost mass flow, which can lead to weight and size increases that ultimately lead to additional drag. Therefore, a device that can reduce or even completely eliminate the need for bleed is highly desirable. Vortex generators (VGs) have been used in many passive flow control applications, such as on wings at subsonic and transonic speeds. Although very effective in delaying or eliminating flow separation, the parasitic drag is large, due to the device height, which is close to

Presented as Paper 2009-4181 at the 39th AIAA Fluid Dynamics Conference, San Antonio, TX, 22–25 June 2009; received 2 October 2009; revision received 25 August 2010; accepted for publication 2 September 2010.

*Postdoctoral Research Associate, Department of Aerospace Engineering. Member AIAA.
†Professor, Department of Aerospace Engineering. Associate Fellow AIAA.
‡Aerospace Engineer. Associate Fellow AIAA.

the boundary-layer thickness. Holmes et al. [2] suggested that a low-profile (sub-boundary-layer scale) VG can produce benefits similar to the traditional VGs while greatly reducing the parasitic drag. In the supersonic regime, a recent computational fluid dynamics study by Anderson et al. [3] using Reynolds-averaged Navier–Stokes simulation (RANS) demonstrated that one particular type of low-profile VG, named microramp, had results comparable with the traditional boundary-layer bleed. They optimized the size and relative length scales based on the downstream boundary layer's incompressible shape factor using RANS numerical methods. However, Ghosh et al. [4] found some significant differences between RANS and experimental results, and their less-empirical hybrid large eddy simulation (LES)/RANS approach yielded better agreement with the downstream experimental data. Similarly, Lee et al. [5] used LES without a subgrid-stress model (LES-nSGS) and found substantial improvements compared with RANS results. The RANS results yielded significant discrepancies in the downstream velocity and pressure profiles with the experiments, which tended to overpredict the boundary-layer thickness, spanwise variations, and shape factors. They also found that reducing the size of the microramps and placing them closer to the impinging shock location reduced the flow separation area and increased pressure recovery downstream. This indicates that the optimum micro vortex generator (μVG) design may be dependent on flow conditions and may require simulations that capture the unsteady large-scale structures.

In this study, spatial and temporal schemes along with different grid resolutions are investigated to capture the detailed unsteady fluid physics. Results are compared with the existing experimental and numerical data. We seek to understand how the development of the vortices generated by the microramp differs under various Mach number conditions (namely, $M = 1.4$, 2.2, and 3.0 with a Reynolds number of $Re_{\delta^*} = 3800$) and to compare that with previous subsonic measurements [6]. In addition, we hope to gain more insight into the impact of the microramps on a turbulent boundary layer at the three different Mach numbers by studying the entrainment of the high-speed fluid and the wake effects of the device. Finally, we hope to understand the behavior of two counter-rotating vortices generated by the device as they travel downstream, by investigating their trajectories and sustainability under different freestream conditions.

II. Numerical Methodology

LES without a subgrid-stress model [7] is used to directly simulate the large-scale structures in this unsteady turbulent flow. Near the wall in a boundary layer, this approach employs only the physical viscosity. In the outer portion of the boundary layer, the flow is virtually free of shear stress, such that turbulence modeling is also unnecessary. Previous investigation [8] has shown that this LES-nSGS approach for a supersonic turbulent boundary-layer simulation gives close agreement to a standard Smagorinsky subgrid-stress model [9] for a supersonic boundary-layer flow at $M = 3.0$ with a Reynolds number similar to that in the present study. The framework of the code is based on WIND [10] (developed at the U.S. Air Force's Arnold Engineering Development Center and the NASA John H. Glenn Research Center at Lewis Field), which is a finite volume solver for compressible flows. The inflow boundary conditions have been modified to generate turbulent boundary-layer flow by employing a rescaling-recycling method for compressible boundary-layer flows based on the method used by Urbin and Knight [8]. This is a computationally efficient method of generating a turbulent inflow condition by avoiding a long computational domain for the spatial development from laminar flow-through transition to turbulent flow. An instantaneous flowfield at a given downstream location is rescaled to fit the frictional velocity and the boundary-layer height for a targeted flowfield upstream. The upstream and downstream planes are denoted, respectively, as the inlet station and the recycle station, and the distance between the two planes should be no less than 1000 wall units to ensure the independence of the turbulent eddy Lagrangian time scale and the periodicity [5,11]. The computational grid is shown in Fig. 1, in which the dimension of the grid is based on the height of the flow control device. The spanwise coordinate z is 0 at the centerline, and the width of the domain is $7.9h$. The height of the grid is $25.9h$, and the normal coordinate y is 0 at the floor. The streamwise length of the domain is $99h$, and the trailing edge of the microramp, which is placed $57.9h$ upstream of the exit plane, provides sufficient distance to study the decay of the streamwise vorticity and the turbulent kinetic energy. The streamwise coordinate x is fixed at zero at the trailing edge of the microramp. The rescale-recycling zone takes nearly 27% of the computational domain, the length of which is $26.6h$, to ensure the development of fully turbulent eddies that are independent of the domain size. The microramp is also shown in the inset of Fig. 1, where the shape and the dimensions are based on the RANS-based optimization results of Anderson et al. [3]. The entire domain is decomposed into 12 zones for parallelization to increase computational speed. The grid-stretching ratio (division of two consecutive cell lengths) in the normal direction to the wall is 1.15, where the first grid point normal to the wall is at $y^+ = 1$, which is based on the shear stress at the inlet station of rescale-recycle zone. Periodic boundary conditions are imposed on the side walls to simulate an array of microramps with a spanwise spacing of $7.5h$ proposed by Anderson et al. [3]. The far-field boundary is specified with the zeroth-order extrapolation. In the following sections, the

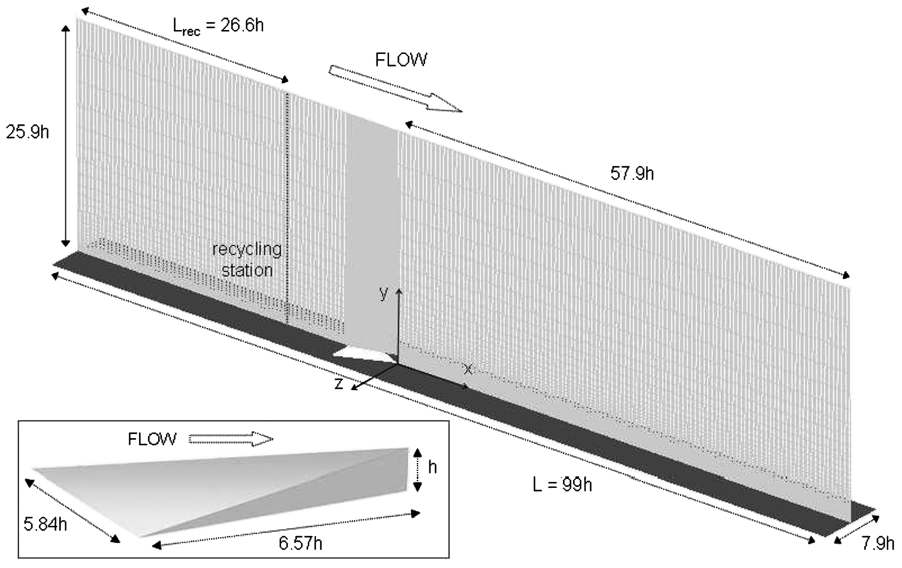

Fig. 1 Computational domain beginning with the recycling zone ($L_{rec} = 26.6h$), where the microramp is placed at the middle of the domain with downstream extension of $57.9h$. The coordinate origin is located at the trailing edge of the flow control device.

numerical scheme study results are analyzed for a turbulent boundary layer, where the domain consists of only the recycling zone from the above domain.

A. Spatial and Temporal Scheme with Limiters

Limiters and spatial schemes were studied using a coarse grid (CG) at $\Delta y^+_{\min} = 1$ with $r = 1.15$, $\Delta x^+ = 28$, and $\Delta z^+ = 13$. The vorticity modulus in the x–z plane at $y^+ = 25$ is shown in Fig. 2. The temporal scheme is the second-order approximate factorization (AF), which was used in the present study, unless stated otherwise. The min-mod [12] limiter with third-order Roe upwind scheme [13] (Fig. 2a) produced structures that were less well developed, showing coarser eddies with no evidence of fine-scale turbulence, indicating that the limiter added significant numerical diffusion. The increase in numerical viscosity can be expected to be similar to an effective decrease in Reynolds number, in which the flow structures are less complex and more diffusive. When the limiter was switched to Superbee [14], the structures were fundamentally changed, in that they were much finer, as shown in Fig. 2b. The refinement of the structures was further enhanced by using a higher-order spatial scheme, fifth-order Roe upwind, as shown in Fig. 2c. This higher-order spatial scheme with Superbee result is comparable with the CG case of Urbin and Knight [coarse monotone integrated LES (MILES) in [8]], as shown in Fig. 2d, and the streak shapes are consistent with the low-Reynolds-number turbulent boundary layer for direct numerical simulation data of Wu and Martin [15]. The same axes and units used in Fig. 2a apply to Figs. 2b and 2c, and those for Fig. 2d are unknown.

The mean streamwise velocity and the Reynolds stress using the min-mod and the Superbee limiters with third-order upwind on the CG are compared with the coarse-grid case of Urbin and Knight [8] and various experimental data [8,16–19] (Figs. 3a and 3b). The temporal averaging employed a time period of $\tau^* = \tau_{\text{int}}/\tau_{\text{dom}} = 8$, where τ_{int} is the total time period of averaging, and τ_{dom} is defined by $\tau_{\text{dom}} = L/U_\infty$, where L is the streamwise length of the domain (Fig. 1), and U_∞ is the freestream velocity. This is twice the averaging previously found to be sufficient to obtain statistical convergence ($\tau^* = 4$) to accurately compare results from different numerical schemes and grid densities [5]. Min-mod yielded higher freestream values of U^+_{VD} (and thus a lower skin friction) than those for Superbee and the results of Urbin and Knight [8], as shown in Fig. 3a. The numerical dissipation produced by the min-mod limiter dampened the fine-scale turbulent structures near the wall, thus underpredicting the wall shear stress. In addition, diffusive and large turbulent structures for the min-mod case (Fig. 2a) yielded a thinner boundary layer, which is shown in Fig. 3b, with a thicker lobe of the streamwise turbulent intensities. The Superbee limiter gave better agreement with Urbin and Knight [8] data and the experiments. Recall from Fig. 2c that the fifth-order upwind scheme captured finer eddies, which improved the shear stress prediction, such that the U^+_{VD} at the freestream was reduced in comparison with the third-order case, as shown in Fig. 3c. The boundary-layer thickness and the peak turbulent intensity yielded a similar reduction as well (Fig. 3d). However, temporal scheme and time-step variations had only a small impact on the mean statistics, as shown in Figs. 3e–3h. The second-order AF is computationally efficient, in that the computation speed is three times faster than the third-order Runge–Kutta and also adds more stability. Time-step variations conducted using fifth-order upwind and AF schemes, similar to the previous cases, gave almost identical results in the mean profiles (Figs. 3g and 3h) for the following time steps: $0.5\Delta t$, $1.0\Delta t$, and $2.0\Delta t$; $1.0\Delta t$ is equivalent to $\mathrm{d}t^* = 0.4$, where $\mathrm{d}t^* = \mathrm{d}t(U_\infty + a_\infty)/\Delta x$, which is the same as the global Courant–Freidrichs–Lewy number (CFL) number. U_∞ and a_∞ are the streamwise velocity and the speed of sound at the freestream conditions, $\mathrm{d}t$ is the time increment, and Δx is the streamwise cell length in the recycling zone. A time step of $\mathrm{d}t = 1.0\Delta t$ is deemed to be a reasonable choice based on the balance of computational efficiency and accuracy after the microramps are inserted in the domain. Based on the results discussed above (Figs. 2 and 3), the numerical scheme choices are as follows: Superbee limiter, fifth-order upwind scheme, and second-order AF with a CFL of 0.4.

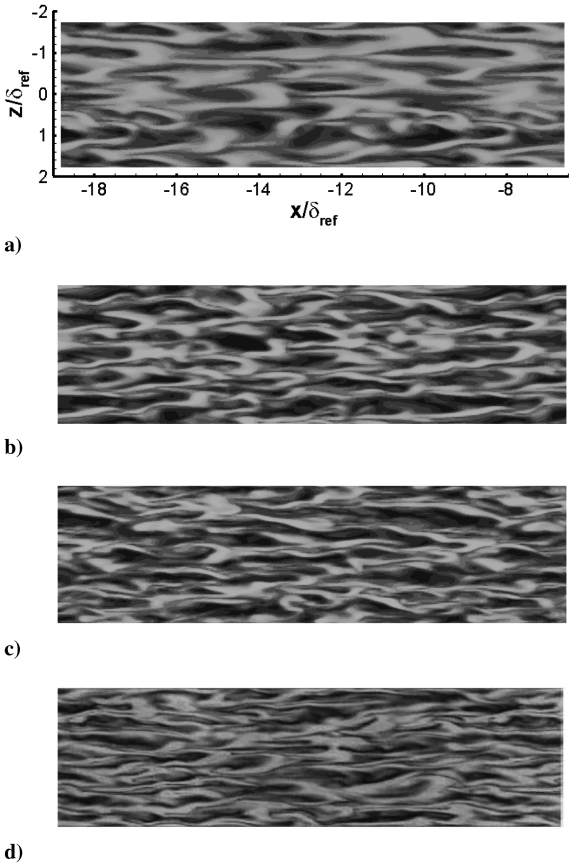

Fig. 2 Vorticity modulus at $y^+ = 25$ for a turbulent boundary layer at $M = 3$ with a CG resolution for present simulations: a) min-mod third-order simulations, b) Superbee third-order simulations, c) Superbee fifth-order simulations, and d) Urbin and Knight [8] simulations with a similar CG resolution using a Riemann solver and second/third-order reconstruction functions.

B. Grid Density

To evaluate the flow solution's sensitivity to the grid resolution, cases doubling the number of grid points in the streamwise direction ($\Delta x/2$), spanwise direction ($\Delta z/2$), and in both directions ($\Delta x/2 + \Delta z/2$) were studied. As shown in Fig. 4b ($\Delta x/2$), Fig. 4c ($\Delta z/2$), and Fig. 4d ($\Delta x/2 + \Delta z/2$), the cases all produced more refined eddy structures than in the Fig. 4a CG result. The same axes and units used in Fig. 4a apply to Figs. 4b–4d. A $\Delta y/2$ case (not shown) gave results similar to those of CG. The $\Delta x/2$ case yielded finer eddy structures in the streamwise direction, whereas the $\Delta z/2$ case yielded similar enhancements in the spanwise direction. The overall refinement of the structures shown by the vorticity modulus for the $\Delta x/2 + \Delta z/2$ case, as expected, gave the most improvement. It would not be wrong to anticipate that the $\Delta x/2 + \Delta z/2$ case would yield more accurate flow solution than in the previous cases, $\Delta x/2$ and $\Delta z/2$; however, the first-order statistics gave an unexpected result, as will be discussed in the next paragraph.

Quantitative results for various grid resolutions are shown in Fig. 5: Reynolds stress for streamwise (Fig. 5a), transverse (Fig. 5b), and spanwise components (Fig. 5c) and the streamwise velocity profiles (Fig. 5d). These profiles are compared with Urbin and Knight [8] CG and dense grid (DG, or baseline MILES in [8]) results, as well as experimental data of Konrad and Smits [19]. The streamwise Reynolds stress approached the Urbin and Knight [8] DG result and the experiments as the grid resolution was refined, shown in Fig. 5a. The differences between the CG result and $\Delta y/2$ are moderate. However, the small discrepancy between the $\Delta z/2$ and $\Delta x/2 + \Delta z/2$ results were unexpected, which indicates that the flow solution

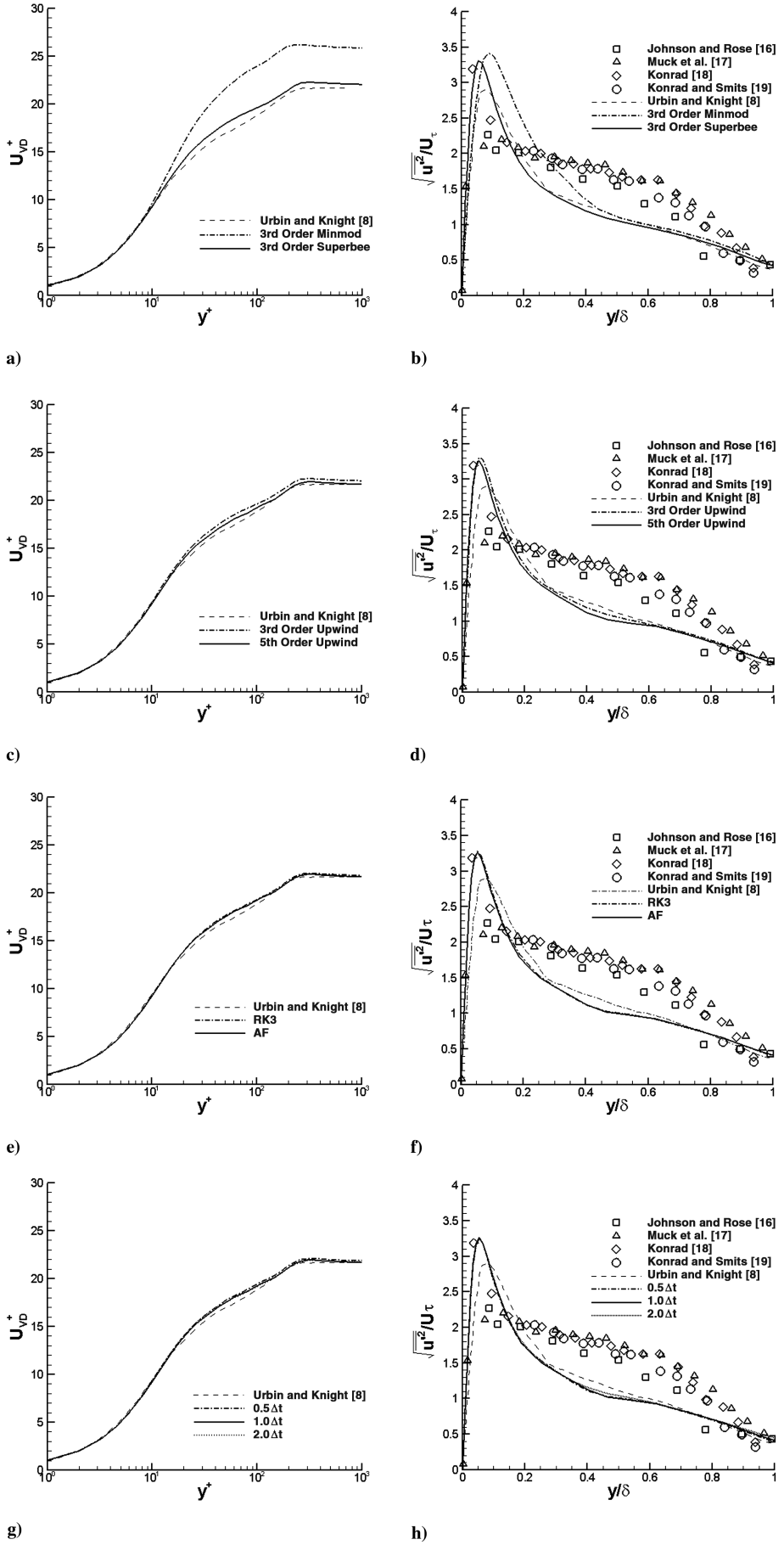

Fig. 3 Numerical scheme study based on the velocity and streamwise Reynolds stress profiles comparing with various supersonic experimental data and Urban and Knight [8] coarse-grid results. Additional information on the spatial and the temporal scheme for each case is as follows: a–b) third-order upwind with AF, c– d) Superbee with AF, e– f) fifth-order upwind with Superbee, and g–h) fifth-order upwind with Superbee and AF.

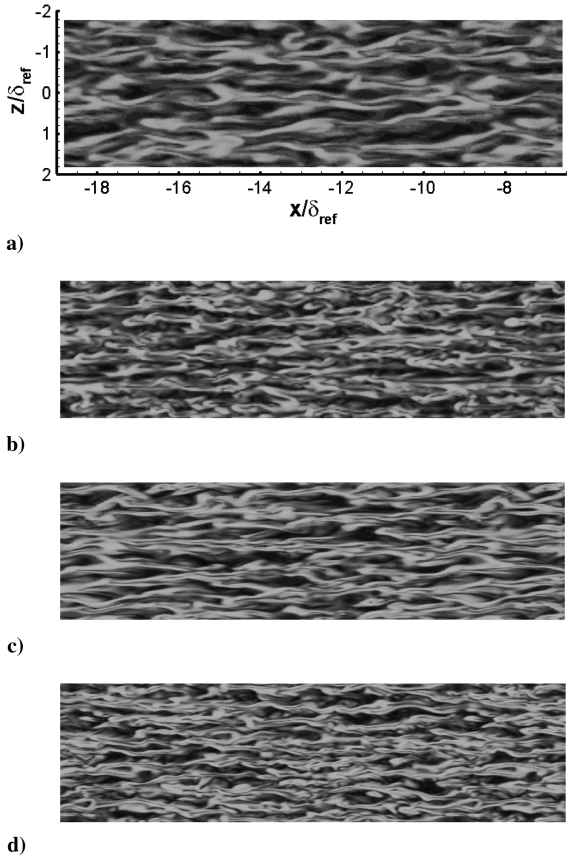

Fig. 4 Vorticity moduli at $y^+ = 25$ for different grid resolutions are shown for turbulent boundary layers at $M = 3$: a) CG $\Delta x^+ = 28$, $\Delta z^+ = 13$, and $\Delta y^+ = 1$ with $r = 15\%$; b) same as CG, except $\Delta x/2$; c) same as CG, except $\Delta z/2$; and d) same as CG, except $\Delta x/2$ and $\Delta z/2$.

has less grid sensitivity in the streamwise direction. The experiments indicated transverse Reynolds stress levels similar to those of the spanwise Reynolds stress (Figs. 5b and 5c), for which the opposite trends are usually seen. Konrad and Smits [19] contributed their results to experimental uncertainties, since the small fluctuations of the transverse and spanwise components are difficult to capture accurately in a supersonic flow. On the other hand, the numerical simulations gave results that are consistent with the expected trends, in that the spanwise Reynolds stress component peak is higher than that of the transverse component (Figs. 5b and 5c). The grid density had a small effect on the Reynolds stress in both the transverse and spanwise directions. The results of the mean streamwise velocity profiles were similar to the streamwise Reynolds stress component, in that $\Delta z/2$ and $\Delta x/2 + \Delta z/2$ cases yielded negligible differences, both of which are intermediate to the CG and DG predictions of Urbin and Knight [8]. Because of the small differences between the $\Delta z/2$ and $\Delta x/2 + \Delta z/2$ cases, the former is chosen as a baseline grid for the present study, since the entire domain after the recycling zone (Fig. 1) is quite large, such that higher grid resolution would be impractical to run several microramp configurations. The grid spacing and the total number of points are summarized in Table 1.

III. Results

Herein we consider turbulent boundary layers at $M = 1.4, 2.2$, and 3.0 with a Reynolds number $Re_{\delta^*} = 3,800$ based on the displacement thickness at the microramp location without the presence of the device. The results here are based on the numerical scheme selected in the previous section: fifth-order upwind scheme with a Superbee limiter and second-order AF scheme with a CFL of 0.4 using the baseline grid. The μVGs are embedded within the boundary layer at the three different Mach numbers. To characterize the impact, the gas dynamic features altered by the presence of the device are first discussed, followed by pressure distributions, and the streamlines over the microramp and its vicinity. Next, the downstream development of a spatially averaged streamwise vorticity and the kinetic energy are investigated, as well as their decay characteristics. Finally, the impact of the Mach number effects on the vortex trajectories are studied and compared with the previous measurements in low-speed subsonic flow [6].

A. Flow over Microramps

Streamwise cuts of the instantaneous density and streamwise velocity contours are shown in Fig. 6 at the midspan ($z = 0$) of the microramp at $M = 1.4$ and 3.0. The shock angle increases at the lower Mach number, where the wake effect decays faster (Fig. 6a) than that at the higher Mach number (Fig. 6b). The high-Mach-number case also shows more density variation in the turbulent wake of the device, which is consistent with increased compressibility effects associated with the wider Mach number range. The velocity changes saw similar effects with the compression wave angle. The flow separation shown in the black region at the trailing edge of the microramp is stronger for $M = 1.4$ (Fig. 6c). On the other hand, the device wake persists longer for the high-Mach-number case, as shown by the large unsteady structures convecting further downstream in Fig. 6d. Despite the differences in the wake structure and their decay, both cases gave similar rise with respect to the floor.

The surface pressure coefficient from an instantaneous LES result (Fig. 7b) is compared with contours generated via pressure-sensitive paint from experiments (Fig. 7a). At the low Mach number, $M = 1.4$, the impact of a high-angle oblique shock can be seen at the leading edge of the microramp for the experimental case as well as the LES result. This effect of Mach number can also be seen by comparing Figs. 7b–7d. As the Mach number increases, the peak pressure coefficient on the ramp surface becomes weaker, which is consistent with theoretical trends for inviscid two-dimensional compression ramps of fixed angle exposed to increasing Mach numbers.

Strong local compression at the leading edge (shown in white) is followed by a reduction in pressure as the flow moves over the ramp for $M = 1.4$ (Figs. 7a and 7b), but not as much for the higher Mach numbers (Figs. 7c and 7d). This indicates that the flow is reaccelerating toward the device trailing edge, as can be seen in Fig. 8a, where an increase in the velocity is observed near the end of the microramp. This acceleration is attributed to the flow spilling over the swept edges. In particular, the low pressure at the ramp side edges (created as the flow spills over and similar to that seen in backward-facing step flows [20]) is communicated to the upper ramp surface because of the modest freestream Mach number and correspondingly high wave angle of the flow. The communication of lower pressure and the spilling of flow over the surface cause the flow to become more parallel with the freestream flow and thus accelerate. In contrast, the fluid velocity on the ramp's surface for the $M = 3.0$ case (Fig. 8b) does not significantly accelerate, due to the higher Mach number, which causes reduced wave angles and thus reduced communication of pressure from the side to the upper surface. In particular, the 24 deg sweep angle of the device suggests that a supersonic flow whose Mach angle is less than this (i.e., whose Mach number is greater than 2.45) will tend to have uniform pressure on the surface. In contrast, flows with higher wave angles (Mach numbers less than 2.45) will tend to communicate the swept-edge pressure-relief effect, to accelerate the flow over the surface.

The magnitude of the low-pressure region on the wall surface just adjacent to the swept sides of the device is also mitigated at the higher Mach number, again because flow cannot be pulled as effectively from the central portions of the ramp surface at lower-wave-angle conditions. In addition, it will be shown later that the vortices shedding off from the device at higher Mach numbers do not roll up as tightly to the device and are thus initially less intense in terms of vorticity when normalized by incoming velocities and ramp heights. Another effect of Mach number is evident downstream of the ramp in terms of pressure distribution along the wall. For the $M = 1.4$ case, there is evidence of a weak recompression shock downstream of the device trailing edge, as shown both by the LES (Fig. 7b) and the experiments (Fig. 7a). In contrast, the higher-Mach-number cases

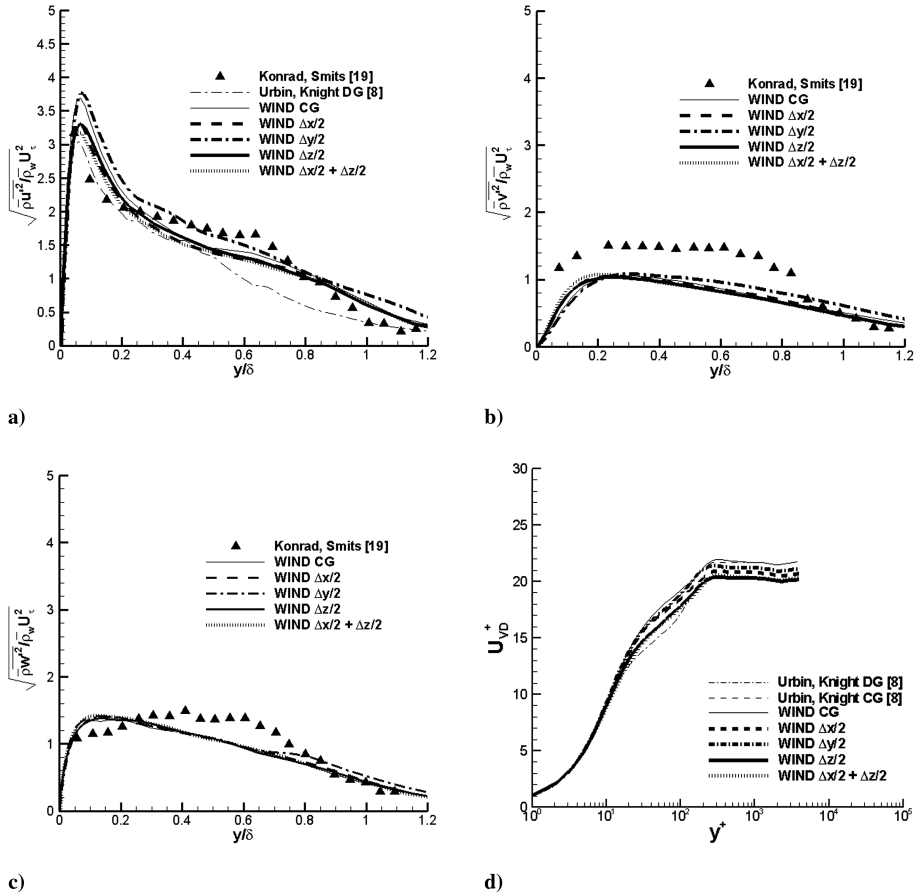

Fig. 5 Reynolds stress of a) streamwise, b) transverse, and c) spanwise components; grid resolution sensitivity is compared with Urbin and Knight [8] CG and DG profiles and with experimental data of Konrad and Smits [19]. Mean velocity profiles are compared in a similar fashion.

(Figs. 7c and 7d) did not yield significant recompression waves after the device.

Streamlines of the flowfield are also helpful to understand the pressure and Mach number distributions. The oil-streak visualization of Herges et al. [21] at $M = 1.4$ and Babinsky et al.'s [22] experiments at $M = 2.5$ are shown in Figs. 9a and 9b with similar microramp heights and can be compared with instantaneous streamlines from the present simulations in Figs. 9c and 9d. The lower-Mach-number case shows that the flow starts turning upstream of the ramp leading edge, which is attributed to upstream communication in the subsonic portion of the boundary layer. Once the flow spills over the swept edge, the vortices tend to roll up tightly along the side edges, and this creates an hourglass feature for the wake flow (see the minimum spanwise extent marked by the arrows in Figs. 9a and 9c). This is attributed to the convection time scale of the fluid elements in the vortices. At lower speeds, the vortices have more time to curl up and rotate for the same given time. In contrast, the path lines are relatively straight in the high-Mach-number case, both upstream of the ramp leading edge and in the wake region, as shown in Figs. 9b and 9d. This can be attributed to reduced communication, with a smaller portion of the boundary layer being subsonic, and to reduced Mach wave angles. The more rapid roll-up of the vortices for the low-Mach-number case shown in Fig. 9c is due to the larger pressure gradient that communicates with the upstream boundary layer via the increased wave angles, pulling in more fluid.

Table 1 Baseline grid spacing and total points

Parameter	Value
Δx^+_{BG}	28
Δy^+_{BG}	1 with $r = 1.15$
Δz^+_{BG}	6.5
Total points	1.1×10^7

B. Turbulent Structure Evolution

Transverse cuts taken at $y^+ = 25$ of the instantaneous velocity (Figs. 10a and 10b), vorticity modulus (Figs. 10c and 10d), and shear stress coefficient (Figs. 10e and 10f) are shown for $M = 1.4$ and 3.0. Upstream of the microramp, the length and the spacing of the low- and high-speed streaks differ slightly for the low- and high-Mach-number cases (Figs. 10a and 10b), due to the changes in the effective Reynolds number. The streamwise (x) and the spanwise (z) extents of the figures range from $-40.5h$ to $57.3h$ and $-3.9h$ to $3.9h$, respectively, for Figs. 10a–10d. The same ranges apply to Figs. 10e and 10f, except for the streamwise extent starting at $x = 0$. The Reynolds numbers based on the freestream conditions are similar for all three Mach numbers, as shown in Table 2. However, the kinematic viscosity at the wall increases for higher Mach numbers, due to compressibility effects, and decreases the Reynolds number based on the wall conditions (Table 2), which contributes to slightly coarser eddy structures. The vorticity modulus had a greater impact from the presence of the microramp at the lower Mach number. The vorticity magnitude was severely reduced in the vicinity of the device (shown in dark regions in Fig. 10c), in comparison with the higher-Mach-number case (Fig. 10d). This is related to the streamlines rolling up quickly and maintaining a close contact on the side walls of the device, as shown in Fig. 9c. Consistent with the microramp wake in Fig. 6d, the long tail structure attached to the trailing edge of the device persists longer for the higher-Mach-number case. Overall, the shear stress field has larger spatial variations near the device trailing edge for $M = 1.4$ (Fig. 10e), where flow separation is evident, shown by the black regions, which is consistent with the white circles in Fig. 9a. The averaging time for the shear stress results (and in all

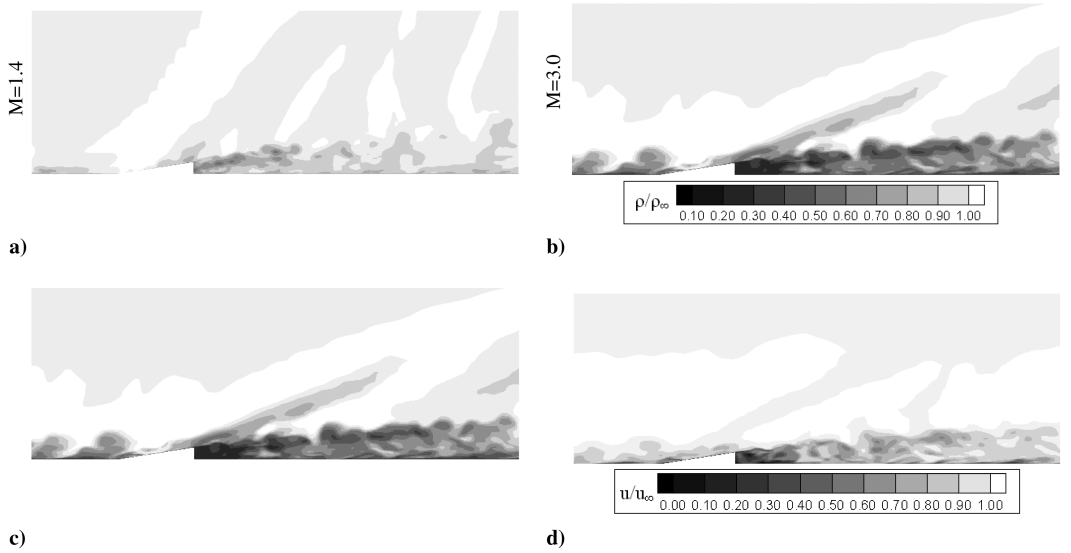

Fig. 6 Streamwise cut of instantaneous density contours at $z = 0$ for a) $M = 1.4$ b) $M = 3.0$ and velocity contours for c) $M = 1.4$ and d) $M = 3.0$. The streamwise (x) and the transverse (y) extent of the figures range from $-14.3h$ to $28.7h$ and 0 to $13.6h$, respectively.

subsequent results) was taken to be $\tau^* = 4$. Despite the wide influences of the microramp at the trailing edge of the device at the lower Mach number, the high shear stress from the primary vortex pair is weaker and does not persist further downstream as in the higher-Mach-number case. Instead, the shear stress recovers more quickly to a uniform spanwise condition (Fig. 10e), which is also evident in the low-speed streaks in Fig. 10a. Consistent with the findings in Fig. 10d, on the other hand, the flow separation indicated by the dark region (Fig. 10f) extends further downstream for $M = 3.0$. High-shear-stress regions (shown in white) are longer and almost parallel to the freestream flow, whereas the white regions in the lower-Mach-number case are pointing outward, due to the recompression shock (Figs. 7a and 7b).

C. Vorticity Strength and Turbulence Kinetic Energy

Spanwise cuts of the mean streamwise vorticity are shown at various downstream locations at $M = 1.4$ and 3.0 in Fig. 11. At the

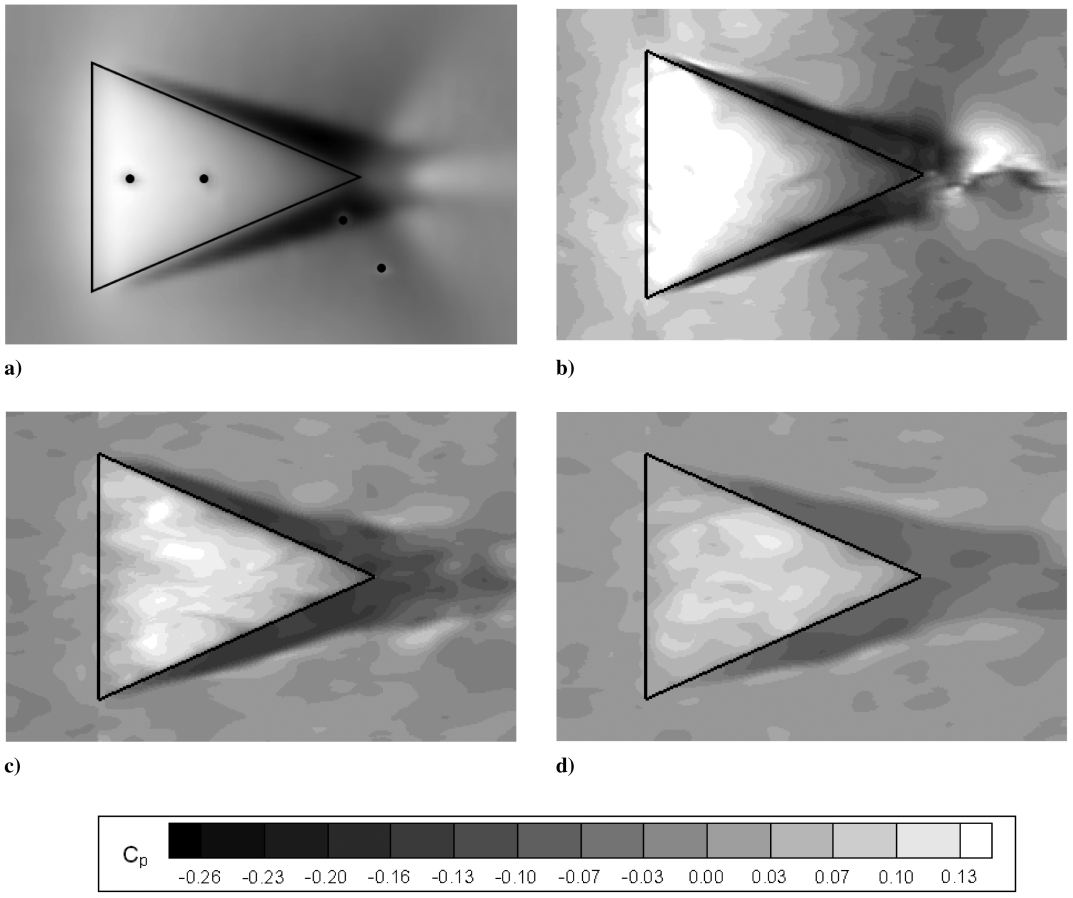

Fig. 7 Wall surface pressure coefficient for a) $M = 1.4$ from experiments using pressure-sensitive paint (black dots are the pressure taps) b) instantaneous LES predictions at $M = 1.4$, c) $M = 2.2$, and d) $M = 3.0$. The streamwise x and the spanwise z extent of the figures range from $-8.8h$ to $3.2h$ and $-3.9h$ to $3.9h$, respectively.

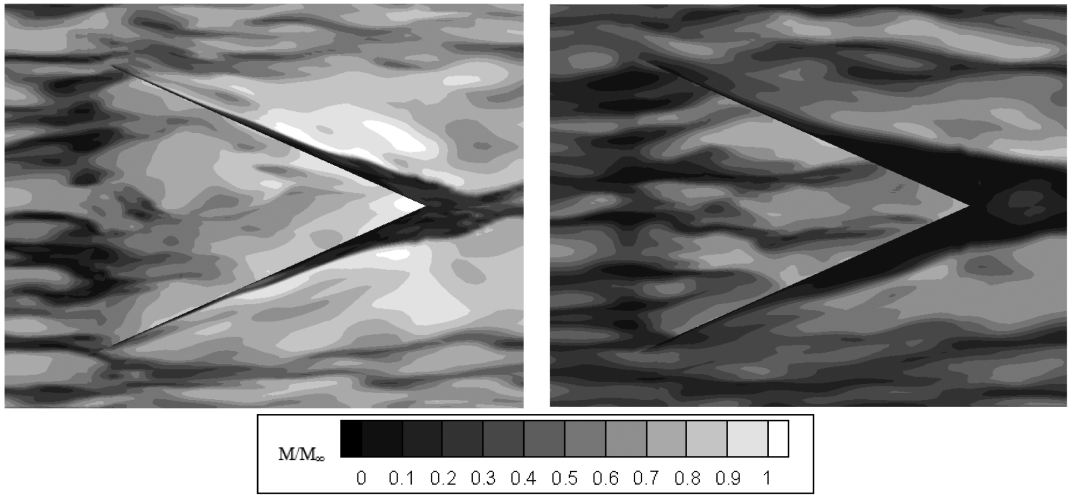

a) b)

Fig. 8 Mach contours of instantaneous LES flow solution at $y^+ = 12$ (above the floor and the top surface of the microramp) for a) $M = 1.4$ and b) $M = 3.0$. The streamwise (x) and the spanwise (z) extent of the figures range from $-8.2h$ to $1.9h$ and $-3.9h$ to $3.9h$, respectively.

lower Mach number, the primary vortices become fully developed faster ($x = 5h$) and rise higher than those of the $M = 3.0$ case and, as will be shown later, the vorticity strength is also greater. The high-speed fluid entrainment is more effective and spreads to a larger region, which can be deduced by the secondary vortices with extended lateral lengths. The two secondary vortices near the wall are almost touching at the middle for $M = 3.0$, whereas there is a small spacing for the lower-Mach-number case. However, the vorticity strength decays faster for the lower-Mach-number case, which may be due to additional dissipation in the close roll-up of the primary vortices (shown in Fig. 9c) and the presence of the recompression shock. The primary vortices have similar heights in both cases; however, the lateral distance between the vortex pair grows larger for the lower-Mach-number case. At $20h$, the primary vortices in both cases have risen well above the floor and their influences on the boundary layer have diminished significantly. In particular, the strength of the primary vortices and the secondary vortices near the wall are significantly reduced for $M = 1.4$, whereas the higher-Mach-number case better retains the streamwise vorticity.

Spanwise cuts of the time-averaged turbulence kinetic energy ($\text{TKE} = (\bar{u}'^2 + \bar{v}'^2 + \bar{\omega}'^2)/2$, where u', v', and ω' are the fluctuating velocity components) normalized by a square of the freestream velocity are shown in Fig. 12 at the same positions. TKE is stronger at $x = 5h$ for the $M = 1.4$ case, which may be due to the tight roll-up of the vortices close to the side walls of the device producing high levels of turbulence. Similar to the vorticity contours in Fig. 11, the overall strength of the TKE decays faster for the lower-Mach-number case, again due to vorticity decay and the presence of recompression shocks. In addition, the effective diameter of the structure, which is

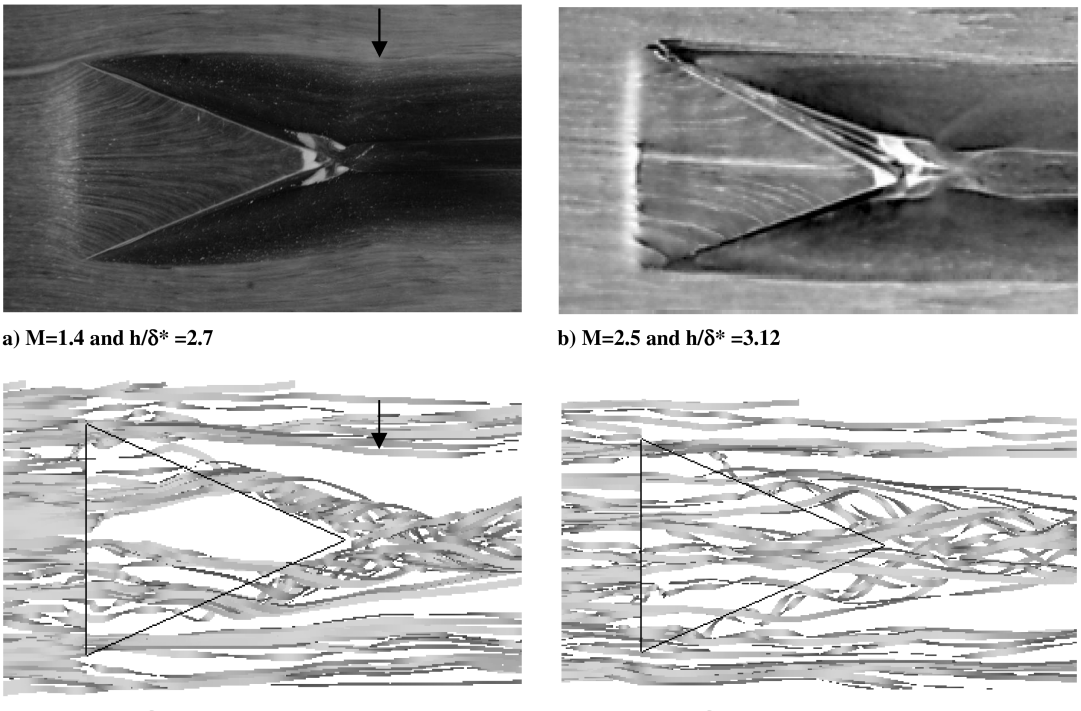

a) M=1.4 and h/δ* =2.7 b) M=2.5 and h/δ* =3.12

c) M=1.4 and h/δ* =3.34 d) M=2.2 and h/δ* =3.34

Fig. 9 Oil visualization (top) [21,22] are compared with instantaneous streamlines of LES (bottom) where each microramp height is similar.

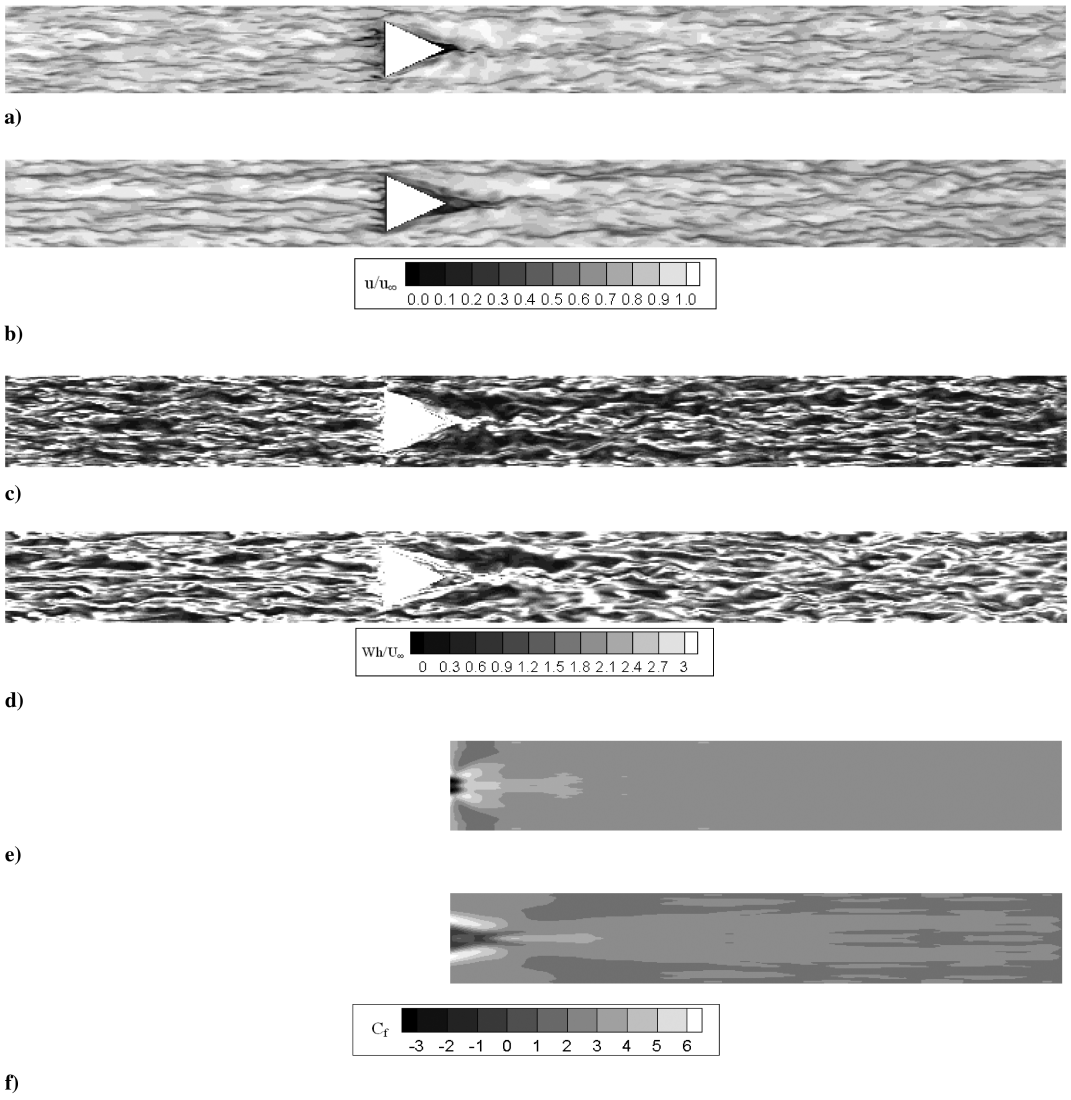

Fig. 10 Low-speed streaks of a) $M = 1.4$ and b) $M = 3.0$; vorticity modulus at c) $M = 1.4$ and d) $M = 3.0$ at $y^+ = 25$; and time-averaged shear stress coefficient (×1000) at e) $M = 1.4$ and f) $M = 3.0$ downstream of the microramp.

composed of the two counter-rotating primary vortices, is greater for the lower-Mach-number case, consistent with the larger spanwise spacing of the vortices. Further downstream ($x = 20h$), the boundary layer in the outward region becomes nearly uniform for both cases, which indicates that the influence of the primary vortices has significantly mitigated.

Spanwise-averaged TKE K is shown at various locations with respect to the position of the microramp for different Mach numbers in Fig. 13. Upstream of the device ($x = -17h$), the K profiles are similar to the square of the streamwise velocity fluctuation profiles, where the differences between each Mach number case are due to small changes in their boundary-layer thickness. At $x = 5h$, the largest effect shown by K due to the microramp is for the $M = 1.4$ case, where the profile has the highest peak, which is consistent with the white regions in Fig. 12. However, further downstream at $x = 20h$, K decayed faster for $M = 1.4$, where the other two Mach number cases still retained some of the structural features of the K profile upstream. At $x = 40h$, K has significantly decayed, and the bulge in the profile has virtually disappeared in the middle region. It is expected that the profile in the middle and the upper regions will continue to decay further and that the peak near the wall will recover back to the $x = -17h$ case.

Correlation of circulation with respect to the effective device height at $5h$ downstream of the microramp is shown in Fig. 14. The line integral for the circulation is shown in Fig. 11 at $x = 20h$ for $M = 3$, which is a square box whose length is half of the microramp's width and extends from the centerline of the domain to capture the primary vortex. The circulation at $x = 5h$ for the three Mach number cases shows the same trend as that of Ashill et al.'s [6] curve fit. The turbulence kinetic energy peaks found in Fig. 13b show similar findings as well. The quantitative discrepancies between the present simulations and Ashill et al.'s experiments may be a result of the different techniques used for computing circulation. A circle with a radius large enough to fit the vortex core (although the core is neither circular nor has a finite radius) was used for the integration in Ashill et al.'s case [6]. However, the integration area in the present simulation is a box and such quantitative comparison is thus difficult. Interpretation of the results is further complicated by the variation in viscosity (from freestream to the wall) for the supersonic flows. This variation leads to differences in wall Reynolds number (and h^+ values) for the LES flows, even though

Table 2 Reynolds number dependence on wall shear stress

Mach number	Re_δ[a]	$\nu_{\text{wall}}/\nu_\infty$	Re_h[b]
1.4	16,700	1.65	330
2.2	17,700	2.83	230
3.0	17,100	4.82	140

[a]$Re_\delta = \rho_\infty U_\infty \delta/\mu_\infty$. [b]$Re_h = \rho_{\text{wall}} U_\tau h/\mu_{\text{wall}}$.

the freestream Reynolds number is constant for the these three cases (Table 2).

D. Vorticity Decay and Vortex Trajectory

Spatially (spanwise and normal directions) averaged streamwise vorticity along the streamwise direction and normalized by the average vorticity at $x = h$ is shown in Fig. 15. The spatial average window is the same square box as that shown in Fig. 11, which may miss some of the vorticity outside of the boundary. As shown in Fig. 13d, TKE is present beyond $Y = w/2$ ($2.92h$), which indicates that the accuracy of the results may have been improved if the average window size had been larger. The secondary vortices rotating in the opposite direction in the vicinity of the primary vortex were mostly filtered, as shown in Eq. (1), such that the only positive streamwise vorticity was included in the spatial averaging scheme. Here, W is the spatial average of the streamwise vorticity ω_x, and the dimension of the window size is $w/2$, which is the half-width of the microramp:

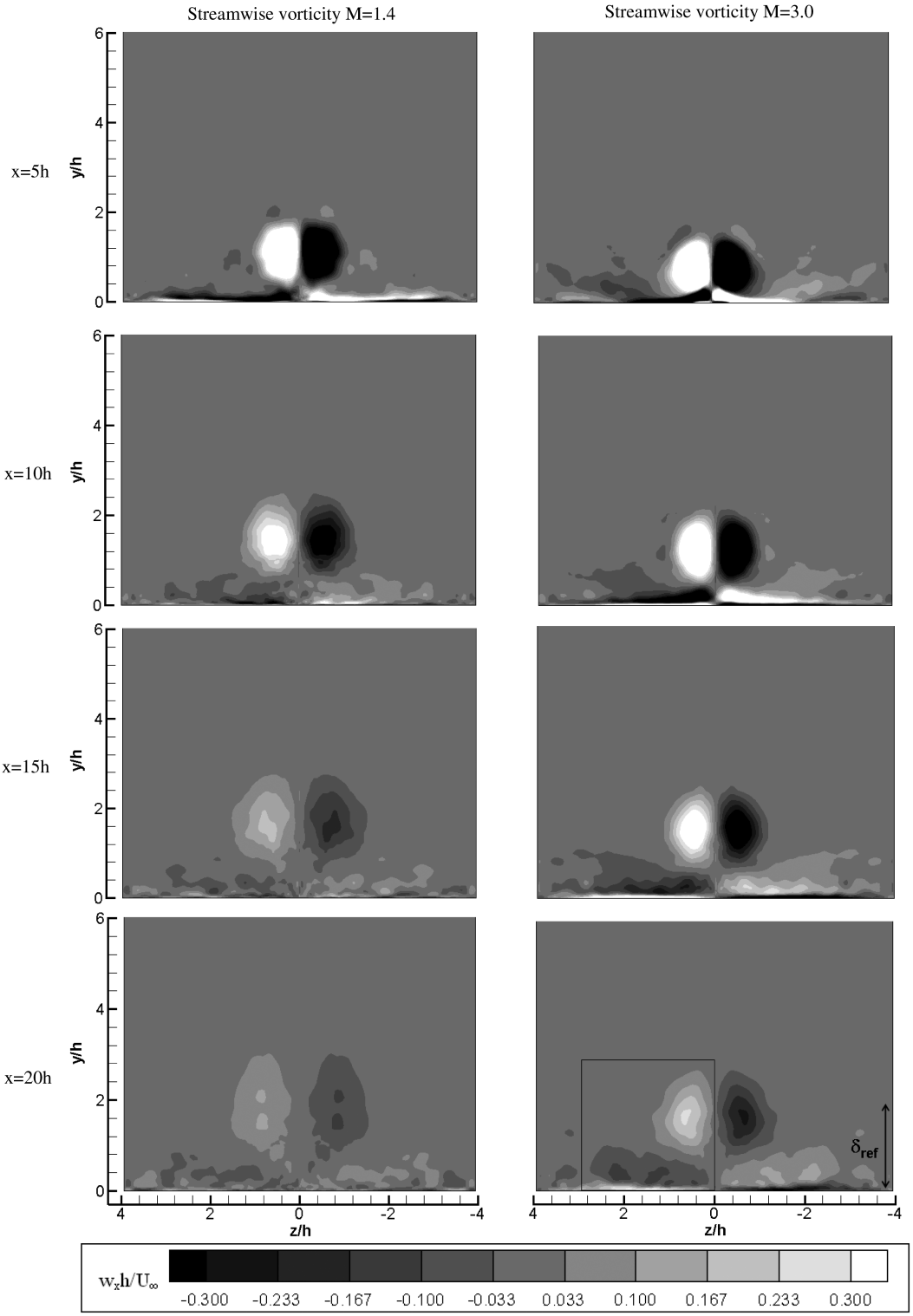

Fig. 11 Spanwise cuts of streamwise vorticity along various downstream locations of the microramp, showing different decay rate for $M = 1.4$ and 3.0. The reference boundary-layer thickness δ_{ref} is indicated by the arrow at $x = 20h$ for the $M = 3.0$ case. In addition, the integration boundary used in Figs. 14–16 is indicated by the box.

$$W = \frac{\int_0^{w/2} \int_0^{w/2} \max(\omega_x, 0)\, \mathrm{d}y\, \mathrm{d}z}{\int_0^{w/2} \int_0^{w/2} \mathrm{d}y\, \mathrm{d}z} \tag{1}$$

In most cases, the positive streamwise vorticity is the primary vortex if the averaging window was placed to the right side of the centerline of the domain, although there were some instances of vortices with positive streamwise vorticity, which are not the primary vortex generated from the microramp. However, the magnitudes of these instances were small, such that the contributions to the average data were negligible.

Consistent with the findings in the previous figures, the initial vorticity strength is higher for the lower-Mach-number case at $x = h$, due to the tight roll-up of the vortices seen at the trailing edge of the device (Fig. 9c). However, the decay speed is accelerated until $10h$ downstream of the trailing edge of the microramp, in comparison with the higher-Mach-number cases, which may be attributed to the increased dissipation generated by the tightly rolled up structure of the vortices. By extension, the loose curls of the vortices for the higher-Mach-number cases, as shown in Fig. 9d, may contribute to less dissipation and thus improve the longevity of the vortices and their strength, as shown in Fig. 15a. However, for downstream distances greater than $30h$, the vorticity strengths converge to a

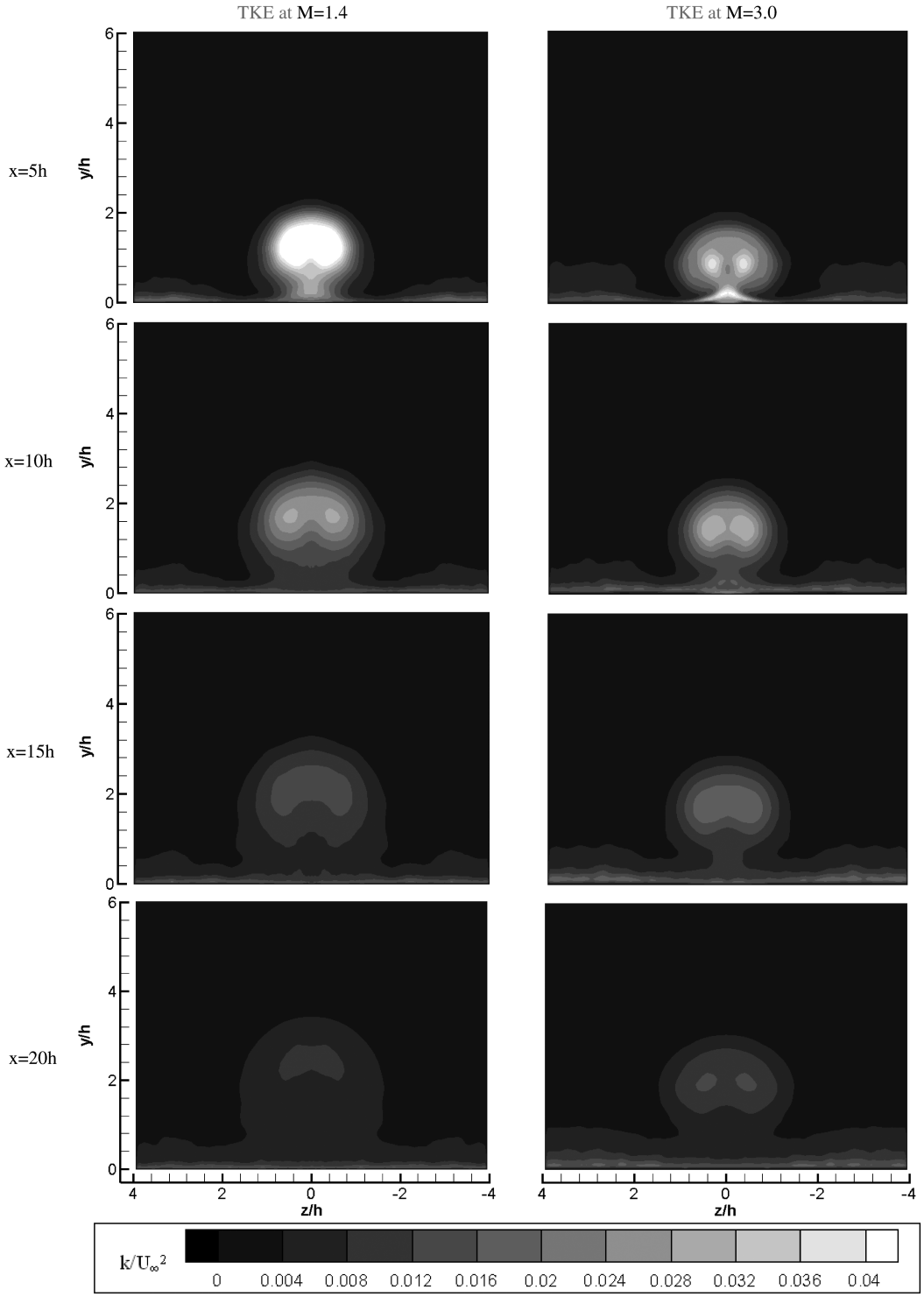

Fig. 12 Spanwise cuts of TKE normalized by the square of the individual freestream velocity shown at various downstream location of the microramp.

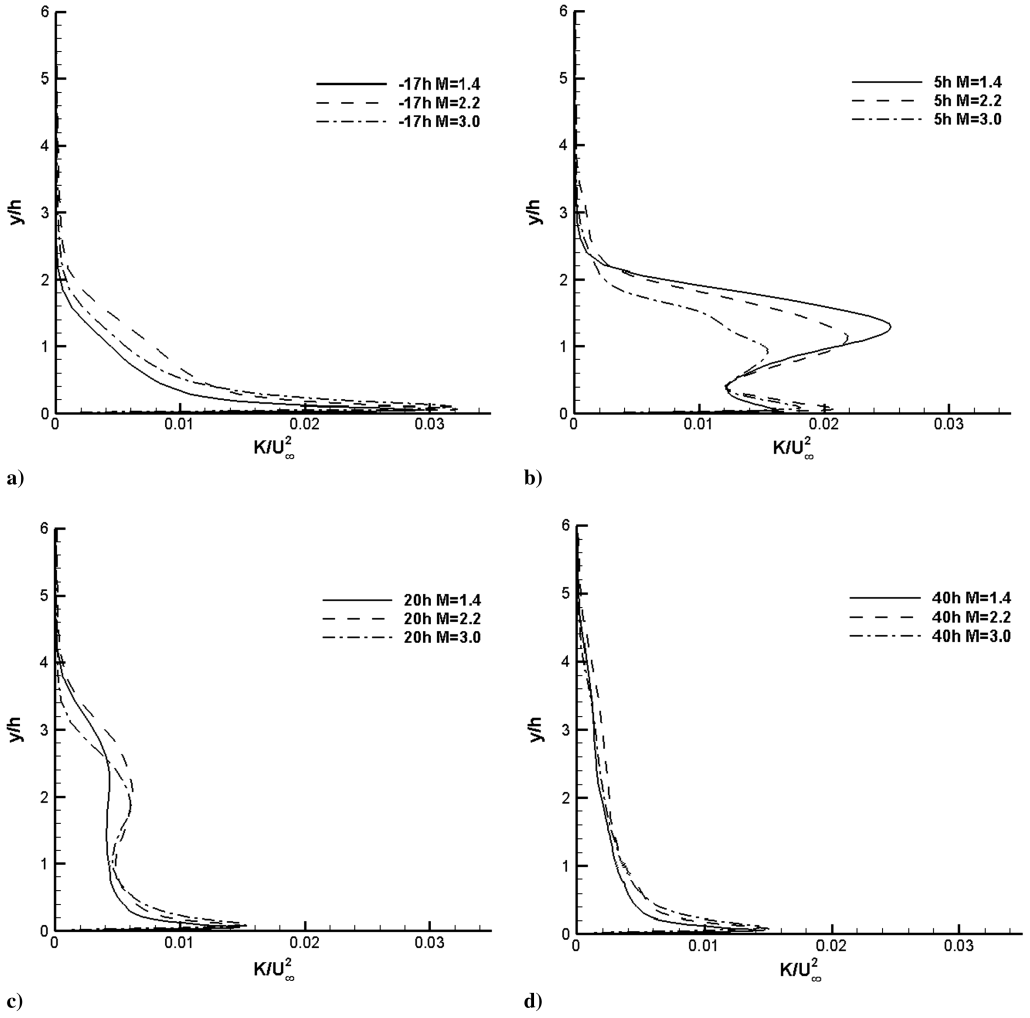

Fig. 13 Spanwise-averaged profiles of TKE at upstream and downstream locations of the microramp for different Mach numbers, where the microramp has the most impact on the lower-Mach-number case.

similar magnitude for all three cases. The log plot of the average streamwise vorticity for the three Mach number cases (Fig. 15b) shows that the decay rate is initially steeper for x-x_{TE} with less than $10h$ for the $M = 1.4$ case, though the rate becomes similar with the higher-Mach-number cases further downstream.

The area-weighted centroids of the vortex core in the normal (Y) and the spanwise (Z) distances, calculated by using Eqs. (2) and (3) with the same averaging window, are compared with Ashill et al. [6] and Babinsky et al. [22] experiments in Fig. 16. In particular, vortex position was estimated based on the vertical and the lateral outer edges of the low-momentum region as

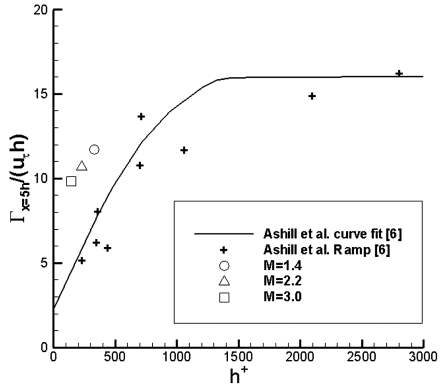

Fig. 14 Correlation of circulation with respect to the effective height normalized in local wall units for various experiments [6] and numerical simulation results.

$$Y = \frac{\int_0^{w/2}\int_0^{w/2} y \max(\omega_x, 0)\,\mathrm{d}y\,\mathrm{d}z}{W} \tag{2}$$

$$Z = \frac{\int_0^{w/2}\int_0^{w/2} z \max(\omega_x, 0)\,\mathrm{d}y\,\mathrm{d}z}{W} \tag{3}$$

The trajectories from Babinsky's experiments were obtained by the present authors from examining the streamwise momentum difference in Babinsky et al. [22]. Error bars of 30% are also shown in Fig. 16 to indicate the expected uncertainty in the estimation of these values. The two counter-rotating vortices generate an upwash motion that self-propels its body to rise higher. The consistent upwash of all the simulations for a wide variation in Mach number (and consistent with experimental results at other Mach numbers) indicates that there is little, if any, effect of Mach number on vortex height (Y/h). However, the Mach number variations had a significant impact on the spanwise distance (Z/h) for the simulations and experiments, where lower Mach numbers were correlated with greater lateral spreads. This trend may be related to the reduction in peak vorticity, which tends to occur as Mach number decreases, as shown in Fig. 15. This hypothesis is consistent with subsonic flow experiments by Ashill et al. [6] for which there was an increased spread in the lateral trajectories for devices that produced higher decay rates of the peak vorticity. This may be due to the increase in overall vortex size as it diffuses, but further studies are needed to better understand this effect, since these results are further complicated by the hourglass paths, which can occur at lower Mach numbers, as shown in Figs. 9a and 9c.

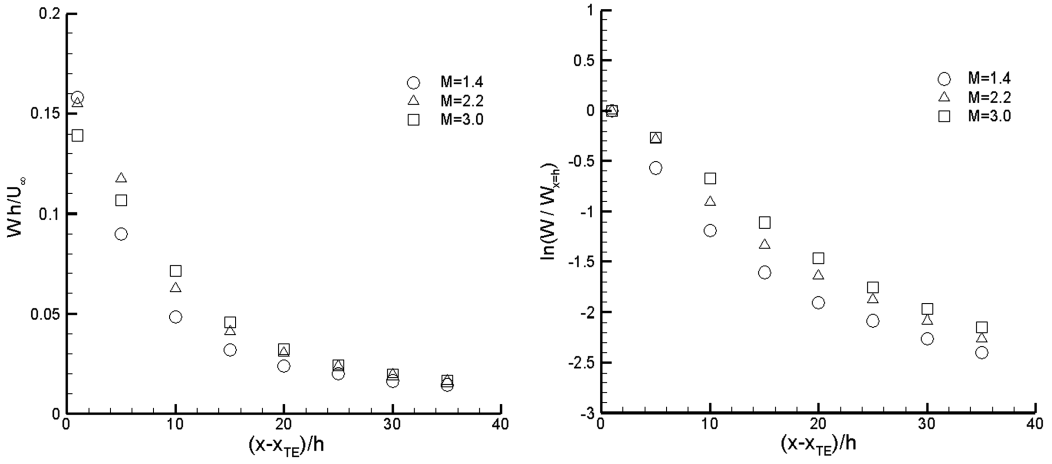

a) b)

Fig. 15 Time-averaged and spatially averaged streamwise vorticity a) decay along the streamwise direction and b) normalized by the averaged streamwise vorticity at h downstream of the microramp displaced in log units.

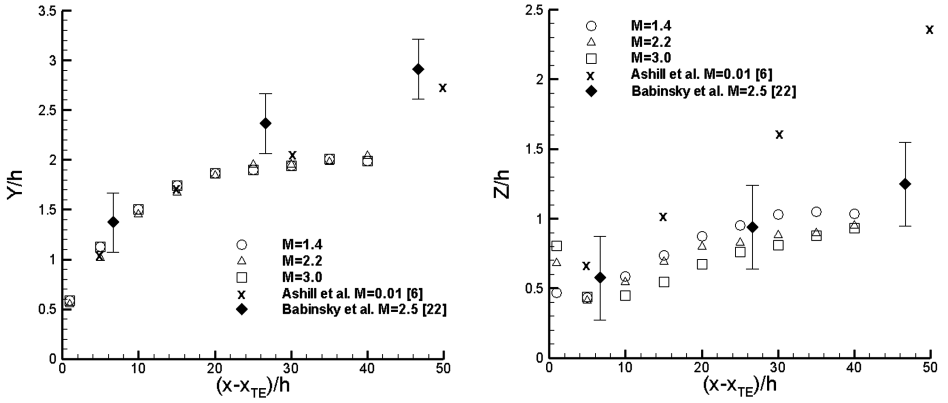

a) b)

Fig. 16 Vortex core trajectory for a) normal and b) spanwise distance for the experimental cases of Ashill et al. [6] and Babinsky et al. [22] and LES study at various Mach numbers.

IV. Conclusions

Mach number effect on turbulent boundary layers with microramps embedded was investigated using LES. An assessment of the available numerical methods was performed and fifth-order Roe upwind differencing with a Superbee limiter, second-order approximate-factorization time discretization with a CFL of 0.3 and moderately dense grids was chosen to provide sufficient accuracy and time efficiency. Both the limiter and the spanwise grid resolution had the most impact on the accuracy of the mean velocity, the Reynolds stress, and the details of the instantaneous flow structure in the present study.

The unsteady density variation in the wake of the microramp was greater for the higher-Mach-number case and persisted longer as well. Strong compression shocks occured at the leading edge of the device for all the supersonic devices, which is typical of two-dimensional ramp oblique shocks. However, this was followed by a reduction in pressure over the surface for the $M = 1.4$ case, as the flow spilled over the side edges of the device and the flow was reaccelerated. This effect was not observed at the higher Mach numbers ($M = 2.2$ and 3.0) and was attributed to the high angle of the Mach wave at $M = 1.4$, which is on the order of the device sweep angle. This allows the upper surface at $M = 1.4$ to communicate with the flow separation region on sides near the trailing edge to pull the flow at the central portions of the ramp surface. As a result, the streamlines traveling past the microramp for the lower-Mach-number case attached closer to the side walls of the device as they rolled up into a vortex pair. Instantaneous velocity and the vorticity modulus field revealed that for low Mach numbers the microramp had a higher local impact on the flow, whereas the long tail structure attached to the trailing edge of the device persisted longer for the high-Mach-number case. Since the microramps have strong local influence at lower Mach number, the vorticity strength is greater near the trailing edge of the device, and this is also consistent with the increased turbulent kinetic energy. However, the turbulent kinetic energy, in the same manner as the vorticity, decays faster for the lower-Mach-number case, which may be related to the tight roll-up of the vortices generating higher dissipation. The improved sustainability of the vorticity magnitude of the microramps at high Mach number suggests that these devices are more effective at high speed. Conversely, the rapid vorticity decay at the lower Mach number flow suggests an increase of the device size in order to extend the flow control device impact further downstream, as these devices have demonstrated to be effective at improving the boundary layer downstream of the shock interaction region [5]. However, further studies will be required to find the optimal configuration. The transverse vortex trajectories show weak correlation with the Mach number, whereas the reduction in Mach number generally yielded an increase in the spanwise distance between the two vortex cores. This could be related to the higher dissipation of the vortices at the lower Mach number, which may cause a growth in the size of the vortices. However, more detailed investigation will reveal further insight into these mechanisms.

Acknowledgments

This work was sponsored by the NASA Fundamental Aeronautics Program, Supersonics Project. The authors wish to thank Bernie Anderson of NASA John H. Glenn Research Center at Lewis Field for technical input, Holger Babinsky of Cambridge University for insight into the flow physics, and the National Center for Supercomputing Applications for the computational resources.

References

[1] Loth, E., "Smart Mesoflaps for Control of Shock Boundary Layer Interactions," AIAA Paper 2000-2476.

[2] Holmes, A. E., Hickey, P. K., Murphy, W. R., and Hilton, D. A., "The Application of Sub-Boundary Layer Vortex Generators to Reduce Canopy Mach Rumble Interior Noise on the Gulfstream III," AIAA Paper 87-0084.

[3] Anderson, B., Tinapple, J., and Surber, L., "Optimal Control of Shock Wave Turbulent Boundary Layer Interactions Using Micro-Array Actuation," AIAA Paper 2006-3197.

[4] Ghosh, S., Choi, J., and Edwards, J., "Numerical Simulations of Effects of Micro Vortex Generators Using Immersed-Boundary Methods," *AIAA Journal*, Vol. 48, No. 1, 2010, pp. 92–103. doi:10.2514/1.40049

[5] Lee, S., Goettke, M. K., Loth, E., Tinapple, J., and Benek, J., "Micro-Ramps Upstream of an Oblique-Shock Boundary Layer Interaction," *AIAA Journal*, Vol. 48, No. 1, 2010, pp. 104–118. doi:10.2514/1.41776

[6] Ashill, P. R., Fulker, J. L., and Hackett, K. C., "Studies of Flows Induced by Sub Boundary layer Vortex Generators (SBVGs)," AIAA Paper 2002-0968.

[7] Fureby, C., and Grinstein, F., "Monotonically Integrated Large Eddy Simulation of Free Shear Flows," *AIAA Journal*, Vol. 37, No. 5, 1999, pp. 544–556. doi:10.2514/2.772

[8] Urbin, G., and Knight, D., "Large-Eddy Simulation of a Supersonic Boundary Layer Using an Unstructured Grid," *AIAA Journal*, Vol. 39, No. 7, 2001, pp. 1288–1295. doi:10.2514/2.1471

[9] Smagorinsky, J., "General Circulation Experiments with the Primitive Equations," *Monthly Weather Review*, Vol. 91, 1963, pp. 99–164. doi:10.1175/1520-0493(1963)091<0099:GCEWTP>2.3.CO;2

[10] Bush, R. H., Power, G. D., and Towne, C. E., "WIND: The Production Flow Solver of the NPARC Alliance," AIAA Paper 98-0935, 1998.

[11] Loth, E., *Particles, Drops and Bubbles: Fluid Dynamics and Numerical Methods*, Cambridge Univ. Press (to be published).

[12] Leveque, R. J., *Finite Volume Methods for Hyperbolic Problems*, Cambridge Univ. Press, New York, 2002.

[13] Roe, P. L., "Some Contribution to the Modeling of Discontinuous Flows," *Large-Scale Computations in Fluid Mechanics*, Lectures in Applied Mathematics, Vol. 22, Pt. 2, American Mathematical Society, Providence, RI, 1985.

[14] Roe, P. L., and Pike, J., "Efficient Construction and Utilization of Approximate Riemann Solutions," *Computing Methods in Applied Sciences and Engineering*, Vol. VI, edited by R. Glowinski, and J. L. Lions, North-Holland, Amsterdam, pp. 499–518.

[15] Wu, M., and Martin, M. P., "Analysis of Shock Motion in STBLI Using Direct Numerical Simulation Data," *Journal of Fluid Mechanics*, Vol. 594, 2008, pp. 71–83.

[16] Johnson, D., and Rose, W., "Laser Velocimeter and Hot Wire Anemometer Comparison in a Supersonic Boundary Layer," *AIAA Journal*, Vol. 13, No. 4, 1975, pp. 512–515. doi:10.2514/3.49739

[17] Muck, K., Spina, E., and Smits, A., "Compilation of Turbulence Data for an 8 deg Compression Corner at Mach 2.9," Princeton Univ., TR MAE-1642, Princeton, NJ, 1984.

[18] Konrad, W., "A Three Dimensional Supersonic Turbulent Boundary Layer Generated by an Isentropic Compression," Ph.D Dissertation, Dept. of Mechanical and Aerospace Engineering, Princeton Univ., Princeton, NJ, 1993.

[19] Konrad, W., and Smits, A., "Turbulence Measurements in a Three Dimensional Boundary Layer in Supersonic Flow," *Journal of Fluid Mechanics*, Vol. 372, 1998, pp. 1–23. doi:10.1017/S0022112098002067

[20] Loth, E., Kailasanath, K., and Lohner, R., "Supersonic Flow over an Axisymmetric Backward-Facing Step," *Journal of Spacecraft and Rockets*, Vol. 29, No. 3, May–June 1992, pp. 352–359. doi:10.2514/3.26358

[21] Herges, T., Kroeker, E., Elliott, G., and Dutton, C., "Micro-Ramp Flow Control of Normal Shock/Boundary Layer Interactions," AIAA Paper 2009-920, 2009.

[22] Babinsky, H., Li, Y., and Pitt Ford, C., "Micro-Ramp Control for Oblique Shock-Wave/Boundary-Layer Interactions," *AIAA Journal*, Vol. 47, No. 3, 2009, pp. 668–675. doi:10.2514/1.38022

J. Sahu
Associate Editor